



Electronic coupling coordinated vanadium nitride/magnesium oxide hetero-junction for accelerating oxygen reaction and long-life flexible zinc-air batteries

Ravichandran Balaji^a, Thanh Tuan Nguyen^a, Muthu Austeria P^b, Do Hwan Kim^b, Joong Hee Lee^{a,c,*}, Nam Hoon Kim^{a,**}

^a Department of Nano Convergence Engineering, Jeonbuk National University, Jeonju, Jeonbuk 54896, Republic of Korea

^b Division of Science Education, Graduate School of Department of Energy Storage/ Conversion Engineering, Jeonbuk National University, Jeonju, Jeonbuk 54896, Republic of Korea

^c Carbon Composite Research Centre, Department of Polymer-Nano Science and Technology, Jeonbuk National University, Jeonju, Jeonbuk 54896, Republic of Korea

ARTICLE INFO

Keywords:

Heterointerface
Vanadium nitride
N-doped carbon
Bifunctional catalyst
Zinc-air batteries

ABSTRACT

Designing highly active, durable, and cost-effective electrocatalysts for oxygen evolution reaction (OER) and oxygen reduction reaction (ORR) is explored as exciting research trends. However, a deep understanding of electrochemical performance enhancement is still a big challenge. Herein, we develop a well-defined vanadium nitride/magnesium oxide (VN/MgO) heterostructure on nitrogen-doped carbon frameworks (VM-NC) with enhanced active sites and tunable electronic structure. The synergistic effect at VN/MgO interfaces facilitates the charge-transfer rate, increases the active sites, and promotes OER/ORR kinetics in an alkaline medium. Theoretical studies suggest that the tuning of electronic structure in VN-MgO effectively boosts the conductivity and catalytic activity of VM-NC. The catalyst delivers an excellent half-wave potential of ≈ 0.852 V for ORR and a low overpotential of ≈ 253 mV for OER. Furthermore, VM-NC-based zinc-air cells (ZACs) exhibit high peak power-density and ultralong cycle-life. The quasi-solid state flexible ZACs present excellent flexibility with different bending states and outstanding electrochemical performance.

1. Introduction

Metal-air batteries (MABs) are considered as promising and effective energy storage alternatives for the next generation of portable and wearable devices. Among various types of MABs, zinc-air cells (ZACs) have attracted high interest, because of their earth-abundant raw material, cost-effectiveness, large-scalable, and high safety concerns compared to the state-of-the-art lithium-ion batteries [1–4]. Despite these advantages, the chemistry of rechargeable ZACs involves the multi-steps of oxygen reactions which mainly cause sluggish reaction kinetics and quickly degrade the electrode performance. These oxygen reactions, which include the oxygen evolution reaction (OER) and oxygen reduction reaction (ORR) continuously occur at the air cathode during the charge/discharge process [5]. Therefore, to enhance the electrochemical performance of ZACs, highly active and excellent durability catalysts for ORR and OER at the air-cathode is required

[6–10]. The prominent electrocatalytic activity of noble metals such as Pt-, Ru-/Ir-based toward ORR, and OER was recognized. However, the large-scale applications were hindered by their high cost, inferior bifunctional activity, and poor durability [11–13]. Therefore, the development of cost-effective bifunctional electrocatalysts with excellent kinetics activities and long-durability is highly essential to implement for commercial ZACs and next-generation wearable energy storage devices.

Recently, transition metal nitrides (e.g., Co_4N , Ni_3N , and VN) have been studied as promising electrocatalysts under alkaline medium owing to their abundant active sites, excellent catalytic activities, low-cost, and tunable electronic structures [14–18]. For instance, Li and co-workers designed a 3D V-doped Ni_3N nanosheet structure via hydrothermal and subsequent nitridation, that exhibited numerous active sites and excellent conductivity with modulating electronic structure. The V-doped Ni_3N possesses outstanding catalytic activity toward HER

* Corresponding author.

** Corresponding author at: Department of Nano Convergence Engineering, Jeonbuk National University, Jeonju, Jeonbuk 54896, Republic of Korea.

E-mail addresses: jhl@jbnu.ac.kr (J.H. Lee), nhk@jbnu.ac.kr (N.H. Kim).

<https://doi.org/10.1016/j.apcatb.2023.122895>

Received 4 March 2023; Received in revised form 30 April 2023; Accepted 18 May 2023

Available online 19 May 2023

0926-3373/© 2023 Elsevier B.V. All rights reserved.

and OER in alkaline electrolytes [19]. Notably, during the OER process, it electrochemically generates oxides and hydroxides compound on the surface of metal nitrides. However, inadequate adsorption energies toward the intermediate species, such as O^* , OH^* , and OOH^* could be the barrier to further transformation reaction, which hinders the activity of the metal nitrides in OER [20–22]. Moreover, heterointerface engineering has emerged as a promising pathway to design electrocatalysts with enriched active sites, tunable electronic nanostructures, and resist to electrolytic corrosion [23–28]. The strong catalyst activities at the heterojunction interfaces could promote defective structures and devote strong electron interaction, which modifies the electron density distribution and boost electron transfer [29–35]. Additionally, the heterointerface enhances electrocatalytic activity by increasing the active sites and high energy defects [36–38]. For example, Yang and co-worker prepared an N, P co-doped CNT confined WN-Ni heterostructure by a simple pyrolysis procedure, which exhibited similar catalytic activities to the state-of-the-art Pt/C for ORR and HER. In addition, the WN-Ni@N, P-CNT requires a small overpotential for OER, compared to IrO_2 . However, their catalyst material suffered from the requirement for long-term durability [39]. Hu et al. developed a transition metal alloys/sulfides heterostructure by controlling from unary to quaternary. The synergistic effect that emerged from the metallic sites in the interfaces could optimize the adsorption/desorption energy barrier and improve the catalytic performance. However, the process required a high sintering temperature and complicated [40]. Peng and co-workers developed a cobalt nitride nanohybrid grown on Ni-foam encapsulated with the N-doped carbon framework (CoN@NC), which demonstrated a self-supporting structure and structural integration. In addition, CoN@NC enables numerous active sites, and the coupling effect of CoN and NC accelerates fast electron and ion transportation, which is beneficial to promote both OER and ORR [41]. However, the highly stable and structural flexibility of these catalysts remains insufficient owing to aggregation and corrosion of the catalyst.

Herein, a facile strategy has been proposed to design a VN/MgO heterostructure on an N-doped carbon framework (VM-NC). The well-defined VM-NC bifunctional catalysts could provide a synergistic effect and improve the oxygen kinetics for OER, and ORR, and increase the performance of rechargeable Zn air cells. The heterojunction between VN and MgO enhances the active sites and catalytic performance by tuning the electronic structure of the catalyst. During the oxygen reactions process, MgO may transform into $MgOOH$, the high catalytic activities of VN could accelerate the conversion reaction. In addition, the interface between metals and N-doped carbon networks promotes electron transfer, which is beneficial to maintain the high activity of OER and ORR. The theoretical studies suggest that the electronic structure tuning of the VN and MgO electrocatalyst effectively boosts the

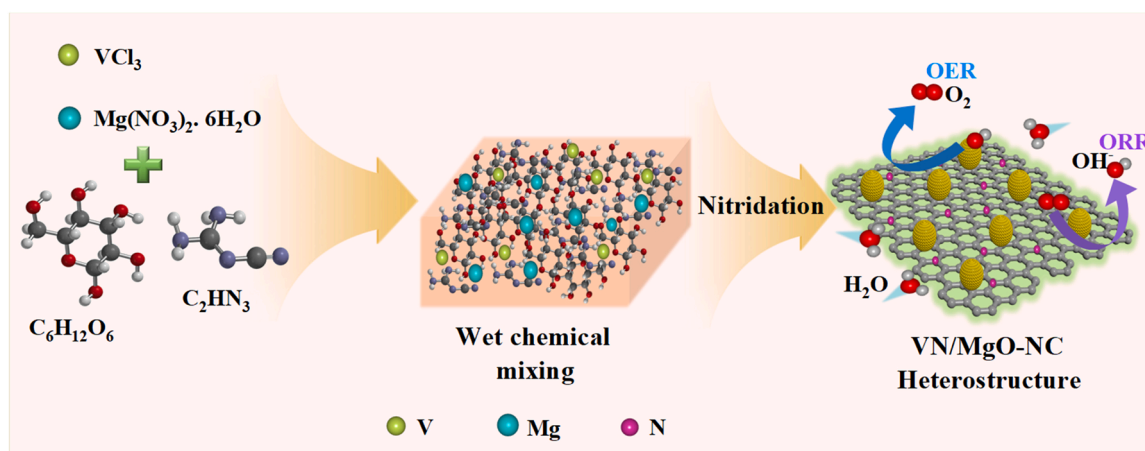
conductivity and bifunctional activity of the VN/MgO catalyst. As the result, the VM-NC catalyst exhibits a low overpotential of ≈ 253 mV at a current density of 10 mA cm^{-2} for OER. Even at a high current density of 100 mA cm^{-2} , the VM-NC catalyst showed a small overpotential of ≈ 410 mV. Moreover, the VM-NC catalyst presents a high half-wave potential of ≈ 0.852 mV, which is comparable to the benchmarked Pt/C (≈ 0.869). When the VM-NC served as the air-cathode, the ZAC delivers a high peak power density of $\approx 165 \text{ mW cm}^{-2}$ at the current density of 250 mA cm^{-2} and exceptional durability for 400 h, which is outstanding to the Pt/C// RuO_2 ZAC. In addition, the quasi-solid state (QSS) flexible ZAC presents excellent flexibility with different bending states with high electrochemical performance, demonstrating the possibility to apply it in flexible and wearable electronic devices.

2. Results and discussion

2.1. Materials characterizations

The synthesis protocol of VM-NC heterostructure is schematically depicted in Scheme 1 via a cost-effective wet chemical method and subsequent nitridation process. Firstly, we dissolved glucose, dicyanamide, and metal sources in DI water at 80°C . Next, the powder was freeze-dried at -80°C and followed by annealing at a high temperature of 800°C under N_2 flow. During the pyrolyzing process, dicyanamide was gradually decomposed at $600 - 650^\circ\text{C}$ and provided the N source to form the VN and further doping into the carbon nanostructure. In addition, the enriched heterojunction between VN and MgO could generate more active sites, further facilitate the adsorption ability, and accelerate the reaction kinetics.

The crystalline and phase structure of the as-obtained material were investigated through the XRD pattern and Raman spectroscopy. In Fig. 1a, XRD pattern of VM-NC heterostructure depicts the strong peaks at 37.6 , 43.7 , 63.6 , and 76.3° , which were determined to the (111), (200), (220), and (311) crystal planes of VN (PDF#01–073–0528) and MgO (PDF#01–074–1225), respectively. Further, the broad diffraction peak at 25.2° represents carbon structure with low degree crystallization. On the other hand, Raman spectra display two vibrational bands (D and G bands) for all N-doped carbon structures (Fig. 1b). The VM-NC heterostructure catalyst exhibits a greater I_D/I_G band of ≈ 1.08 than VN-NC (≈ 0.99) and MgO-NC (≈ 1.05). The higher ratio I_D/I_G band value of the VM-NC catalyst is associated with the carbon lattice distortion by N atoms, which promotes ion transportation kinetics and electrochemical phase transitions [42,43]. In addition, the Raman spectral mapping indicates the higher I_D/I_G ratio of VM-NC heterostructure in compared to VN-NC and MgO-NC that is the result of heterostructure formation process, and that expected to increase the electrochemical



Scheme 1. Synthesis protocol illustration of VN/MgO heterostructure electrocatalyst.

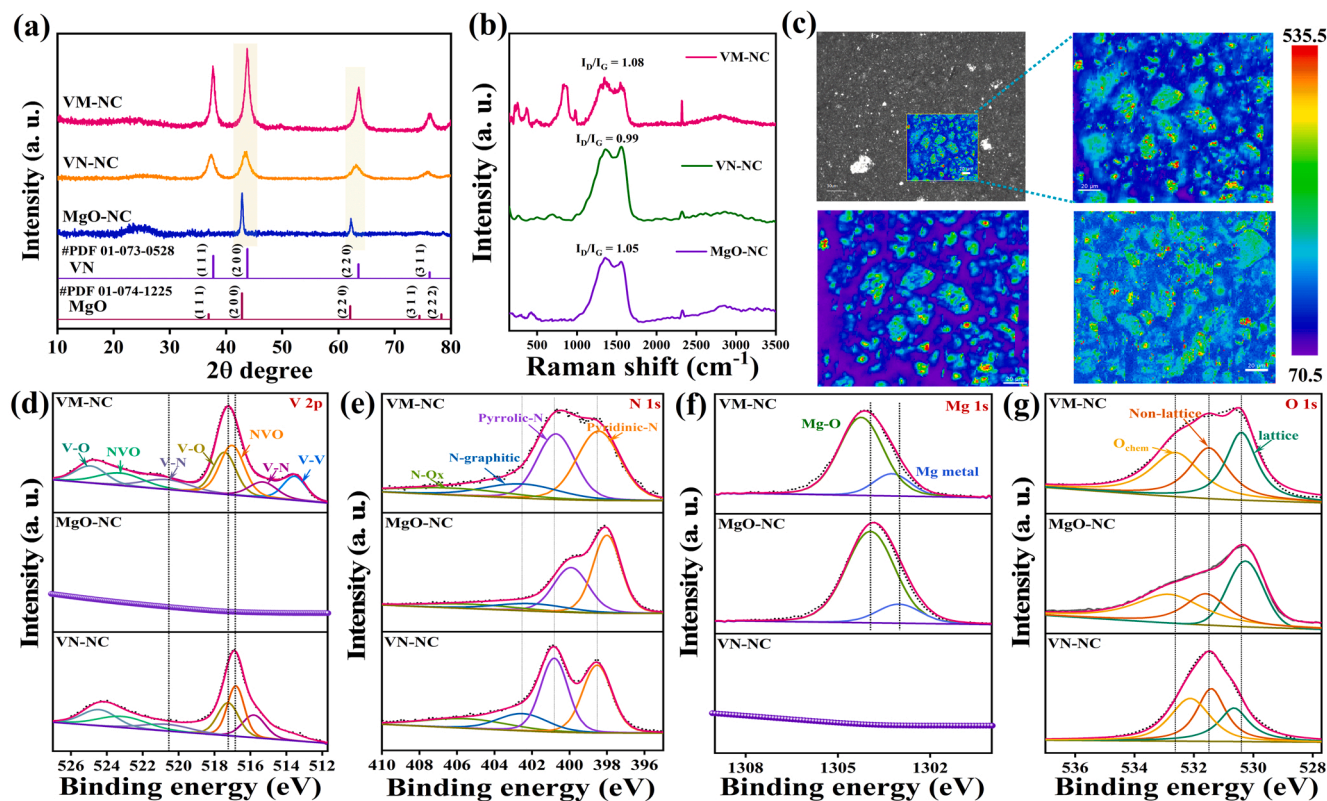


Fig. 1. (a) XRD patterns; (b, c) Raman spectra and Raman images; (d-g) XPS analysis of as-synthesized VM-NC heterostructure, VN-NC and MgO-NC electrocatalyst.

performance (Fig. 1c). On the other hand, the VM-NC catalyst possess a high peak at the wavenumber of 800 cm⁻¹ corresponds stretching vibration of symmetric and asymmetric V-O-N bond, which arises from the heterogenous interface formation [44]. The peak positioned at 943 cm⁻¹ attributed to stretching modes of terminal oxygen (V-O) bonds, which determine the unshared oxygen, respectively [45,46]. The corresponding peak at the wave number of ≈ 252 and 373 cm⁻¹ related to the Mg-O vibration in the VM-NC, which is negatively shifting in comparison to MgO-NC due to the formation of heterostructure (Fig. S1) [47].

The chemical valence and surface state of the as-prepared electrocatalysts was examined through X-ray photoelectron spectroscopy (XPS) analysis. The XPS survey curve revealed the presence of V, Mg, N, C and O elements which was depicted in Fig. S2. The high-resolution XPS of V 2p was deconvoluted into V 2p_{3/2} and V 2p_{1/2} (Fig. 1d). The V 2p_{3/2} revealed the three major peaks which are attributed to the V-V (≈513.3 eV), V-N (≈515 eV), N-V-O (≈517.2 eV), and V-O (≈517.1 eV), that are ascribed to the V³⁺, and V⁵⁺ species of heterostructures. Similarly, the V 2p_{1/2} revealed the peaks at binding energy of 520.8, 523.5, 525 eV, which attributed to the V-N, N-V-O, and V-O bonds, respectively [48]. The appearance of oxides states on V species owing to the unavoidable surface oxidation and oxygen bonded from MgO at the interfaces. The N 1s spectrum of VM-NC is deconvoluted into four peaks of pyridinic N (398.2 eV), pyrrolic N (400.3 eV), N-O_x (405.4 eV), and graphite N (402.1 eV), respectively (Fig. 1e) [49,50]. As shown in Fig. 1e, the corresponded peaks in VM-NC exhibited a negative shift toward the VN-NC due to the successful formation of VN-MgO heterostructure that tune the electronic configuration and increase the active sites of the catalysts [51]. The Mg 1s spectrum is deconvoluted into two peaks of Mg-O (1304.2 eV) and Mg metal (1303.2 eV) (Fig. 1f), which verifies that Mg atoms are well-bonded with the O in the heterostructures. Moreover, a slight shift toward higher binding energy was detected in the heterostructure due to stress occurring between the atoms and heterointerfaces [52,53]. The high-resolution O1s spectra are

classified into three major peaks of lattice, defect, and adsorption of oxygen on the surface of materials (Fig. 1g). The lattice oxygen peak at binding energy of 530 eV verifies the formation of MgO in heterostructures. Moreover, the defect of oxygen arises during the pyrolysis process at binding energy of 531.1 eV, which could enhance the adsorption of intermediate species and enhance the electrochemical performance of the catalysts [54]. The peaks at binding energy of 532.3 eV owing to the unavoidable adsorption of oxygen species which was detected during the XPS measurement. The high resolution of C 1s spectra for all as-prepared materials reveal four major peaks, which are associated with C-C (284.5 eV), C-N (286.4 eV), C-O (288.9 eV), and C=O (290.9 eV) bonds, respectively (Fig. S3) [55]. These results further confirmed the successful formation of N-doped carbon framework [56]. In addition, the weight percentage of each element in as-prepared material was shown in Table S1 further confirmed the successful formation of nanostructures. Furthermore, the Fourier-transform infrared (FT-IR) spectroscopy of all as-prepared materials was examined and shown in Fig. S4. The typical peak at the wavenumber of ≈ 581.4 cm⁻¹ represents the frequency stretching of Mg-O, demonstrating the existence of MgO in the VM-NC heterostructure and MgO@NC nanostructure [57].

2.2. Theoretical calculations

Density functional theory (DFT) calculations are used to predict the structural and electronic properties of the MgO, VN, and heterostructure materials [58,59]. Initially, the bulk material of MgO and VN was optimized (Fig. 2a). The molecular unit of cubic MgO is MgO₆ which means that it has a very symmetrical octahedral structure and the molecular unit of cubic VN is VN₄, which shows that it has a perfect tetrahedral structure. Furthermore, the heterostructure material (a mixture of MgO and VN cubic phases) was optimized, and it shows that the MgO₆ and VN₄ units are substantially distorted compared to the pure phases. The MgO₆ unit of VN/MgO heterostructure undergoes tetragonal distortion and transforms into C_{4v} symmetry. Whereas the VN₄ unit

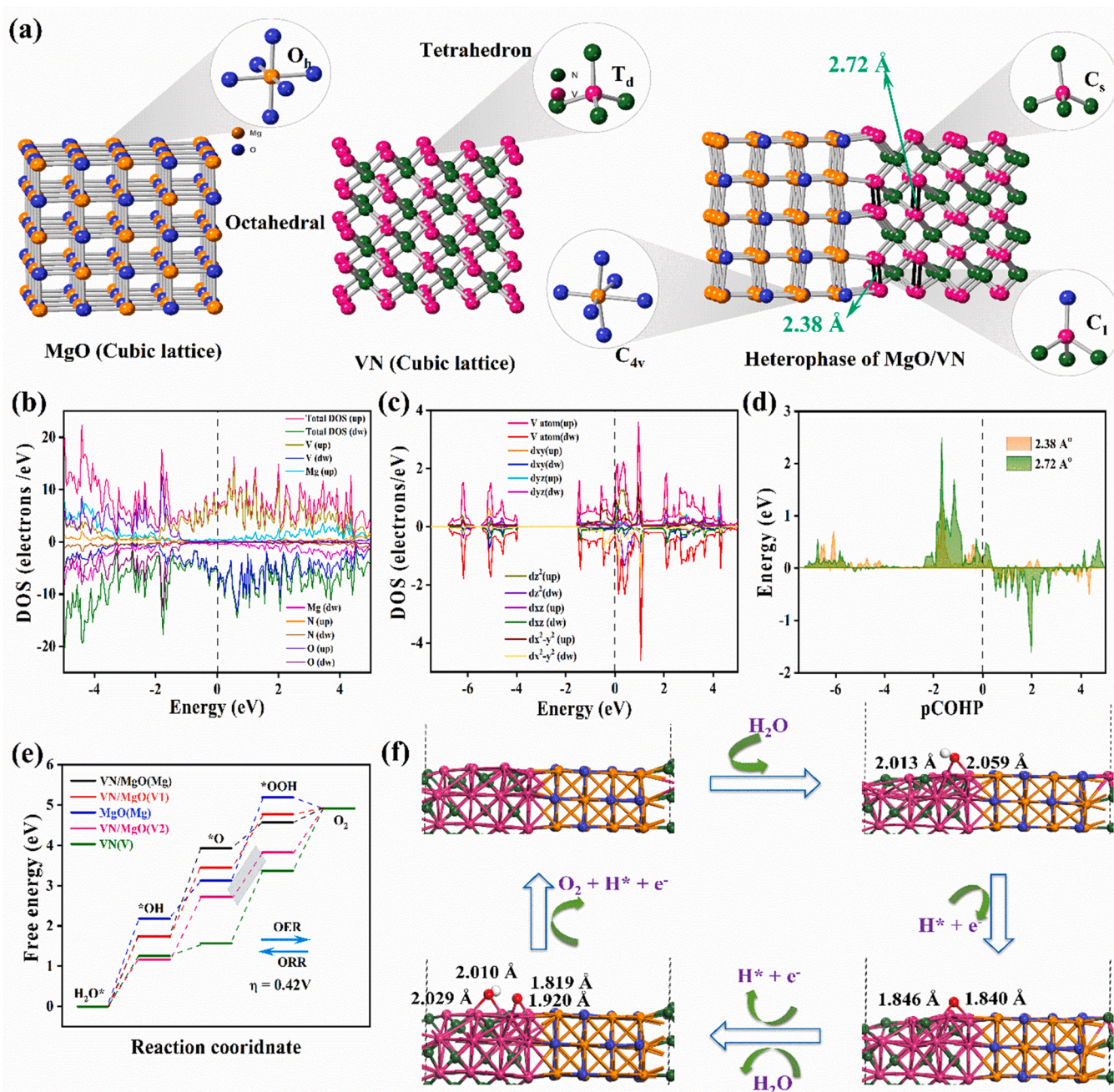


Fig. 2. The optimized bulk materials have been shown along with the repeating molecular unit (a) MgO, VN, and heterostructure of MgO/VN phase, (b) Calculated atom projected density of states (DOS) for VN/MgO heterostructure, (c) The project d orbital population of V atoms in heterostructure of VN, (d) V-V bond in VN/MgO heterostructure, (e) Free energy calculation of all samples for OER/ORR, and (f) Catalytic mechanism for OER of VN/MgO heterostructure.

has been transformed into a highly distorted unit denoted as C_s symmetry. The bond length and angles around the metal centers are tabulated (Table S2). In the heterostructures, the length of the V-N bonds is shorter than in a VN cubic lattice. Internal strain in the heterostructure of VN/MgO causes the formation of a V-V bond that may enhance the electrocatalytic activities by increasing the conductivity. Crystal Orbital Hamiltonian Population (COHP) analysis shows the broadening of the peak of V-N bonds in the heterostructure of VN/MgO than VN lattice due to the enhancement of covalent nature and resulting that the reduction of V-N bond length has been observed (Fig. S5 & Table S3). On the other hand, the Mg-O bond is weakened due to the heterostructure formation; COHP graph indicates that the antibonding nature of the Mg-O bond has been observed near Fermi and that was not found at the pure MgO lattice (Fig. S6). At the same time, the COHP analysis has

confirmed that V-V bonds form at heterostructures and the population enhanced at the Fermi level shows that the formation of V-V bonds is a major factor in the catalytic properties. (Fig. 2d). These results were confirmed by the iCOHP values, which show that the covalent nature of V-N and the formation of V-V bonds will have an effect on the electrocatalytic properties.

The Mulliken and Löwdin population analysis has been performed for all three lattices, and it shows that the fraction of Mulliken charge of V has been enhanced at the heterostructure of VN/MgO than in the VN lattice. At the same time, the decreasing charge of the O in MgO/VN lattices than MgO crystal structure. This illustrates that the fraction of charge transfer that occurs from MgO to VN lattice is enhancing the catalytic nature of VN/MgO heterostructure (Table S4). Further, the atom projected density of states (PDOS) calculations have been performed

for MgO, V, N and VN/MgO lattices. MgO has a wide bandgap and is a semiconductor (Fig. S7a), while VN is metallic in nature (Fig. S7b). However, VN/MgO heterostructure lattice shows that the population has been enhanced at the fermi level, particularly the population of V atoms are found more than Mg atoms (Fig. 2b). It clearly indicates that the V atoms play a major role in the catalytic properties. Moreover, the d -orbital projected DOS of V atom in VN/MgO heterostructure illustrates that a significant amount of dz^2 orbital population was obtained at the fermi (Fig. 2c). It shows that heterophase can serve as good active sites because the z -oriented orbital can interact more with the adsorbates.

Moreover, we have performed the theoretical work function for all models and the results are shown in Fig. S8. The work function of VN/MgO heterostructure displayed a small value of 2.74 eV, which is lower than other counterparts of MgO (4.54 eV) and VN (3.7 eV), respectively. A lower work function of VN/MgO heterostructure indicates a lesser activation barrier for electron donation from the surface of the electrocatalyst to the reactant [60].

The synergistic catalytic effect of VN/MgO is investigated whose free energy evolutions are presented in Fig. 2e-f. The adsorption free energies for OOH^* , OH^* , and O^* intermediates were examined based on four-electron ORR and OER mechanisms to determine the overpotentials (for more details in methodology part). All the intermediates are stably adsorbed at the V sites of the VN/MgO heterojunctions, as illustrated in Fig. S9. The ORR process can be viewed as the inverse of the OER process. The smallest free energy of *OOH formation and dissociation are

established as the rate-determining steps for OER and ORR reactions. Moderate adsorption interactions with the key *OOH intermediates were found in VN/MgO heterojunction exhibits superior bifunctional OER/ORR properties in the electrocatalytic process with lower overpotentials ($\eta_{\text{OER}} = 0.42$ V and $\eta_{\text{ORR}} = 0.51$ V) compared to other VN and MgO structures (Table S5).

For MgO (200), the interaction between the *OOH adsorbate and MgO is weak (Mg-O: 2.935 and 3.587 eV in Fig. S9a), which makes it not favorable for OER and ORR electro catalytic reaction. On VN (111), where the length of the V-O bond is 1.662 (Fig. S9b), strong oxygen binding has been seen. it prohibits the reversible reaction. While in the case of heterojunction (VN/MgO), the moderate bond length between the surface and the adsorbates makes it reversible for electrocatalytic processes (Fig. S9c-d).

2.3. Morphological characterization

The morphological characteristics of VM-NC heterostructure were examined through SEM and TEM. In Fig. 3a-b & Fig. S10, the SEM and TEM images clearly show uniformly distributed VN and MgO nanoparticles on nanoporous carbon networks. These porous carbon networks can enhance electron transport kinetics with a large accessible surface area and OER and ORR kinetics performance. Moreover, the VM-NC nanoparticles play the role as the main active site for electrochemical performance which is involved in the OER and ORR. The SEM-EDS color

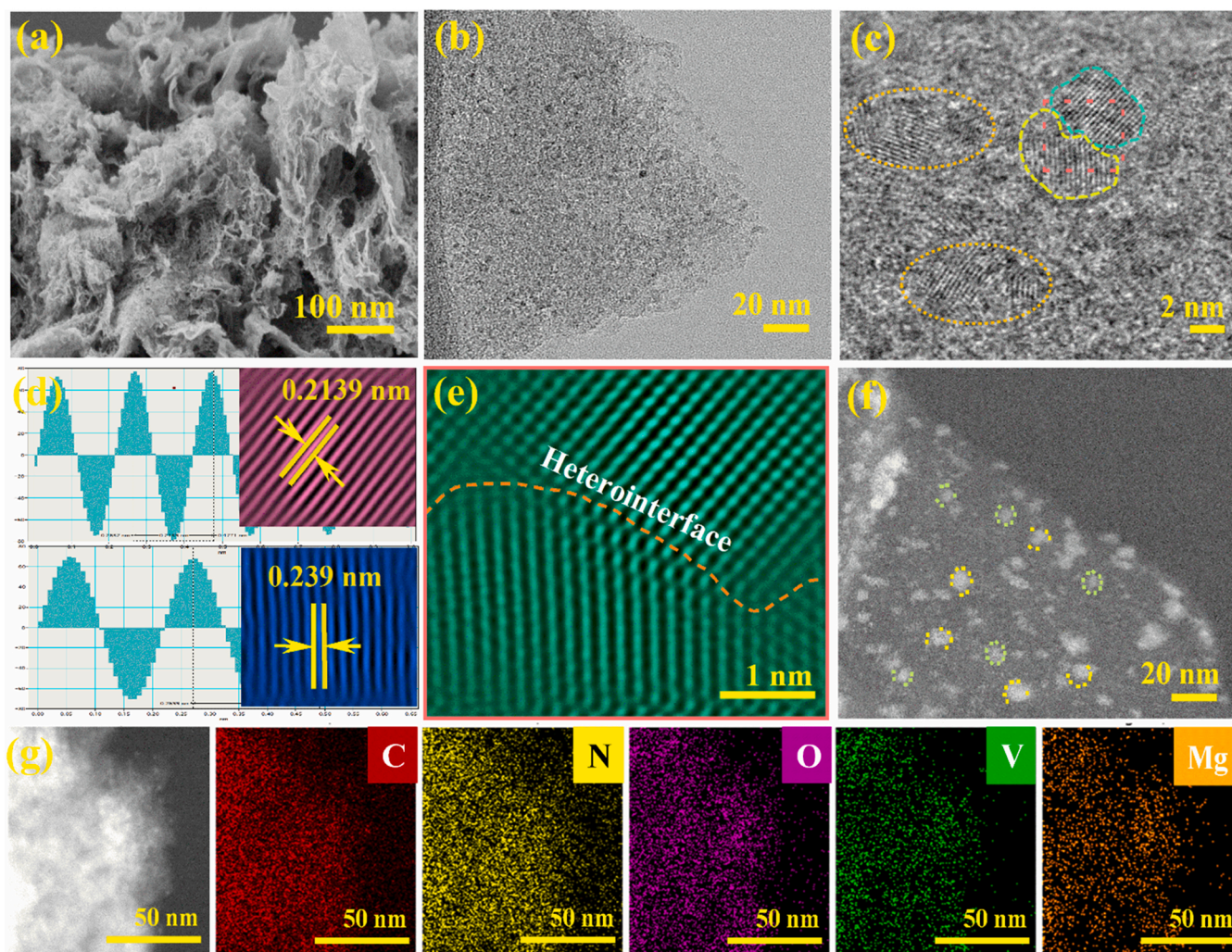


Fig. 3. Topological characterizations of VM-NC heterostructure. (a) FE-SEM, (b, c) TEM images. (d) interplanar spacing of VN and MgO, (e) lattice planer of heterointerface (f) STEM image of VM-NC heterostructure, and (g) TEM elemental mapping of VM-NC heterostructure.

mapping with the presence of elemental V, Mg, C, N, and O species was depicted in Fig. S11, which revealed the uniform distribution of each element. The HR-TEM images clearly presented boundary with the different phases corresponding to VN and MgO in Fig. 3c. Fig. 3d,e clearly shows the lattice fringes of 0.239 and 0.214 nm that are assigned to (111) and (200) facets of VN and MgO, respectively. The STEM image displays the presence of vanadium and magnesium atoms with different contrasts (Fig. 3f). Moreover, the STEM-EDS color mapping further confirms the distribution of V, Mg, O, N, C elements in VM-NC heterostructures (Fig. 3g). The structure tuning of VM-NC could provide the enriched active sites and long-term stability electrocatalyst.

2.4. Electrocatalytic performance (ORR and OER)

The electrocatalytic performance of VM-NC heterostructure catalyst towards ORR was evaluated using a rotating disk electrode (RDE) and rotating ring-disk electrode (RRDE) under 0.1 M KOH solution. Firstly, the cyclic voltammetry (CV) of VM-NC was carried out at the scan rate of 5 mV s^{-1} in the potential range from 0.2 to 1.2 V vs. RHE. The CV curve showed a sharp reduction peak at the potential of $\approx 0.8 \text{ V}$ vs. RHE in the O_2 -saturated electrolyte (Fig. S12), demonstrating the excellent ORR activity of VM-NC. In contrast, no significant peak was observed for CV measurement under an N_2 -saturated solution. To further examine the activities of the VM-NC catalyst, we performed the linear sweep voltammetry (LSV) at a rotation speed of 1600 rpm (Fig. 4a). The VM-NC exhibits the onset potential of 0.93 V vs RHE and a high half-wave potential of $E_{1/2} = 0.852 \text{ V}$ which is better than VN-NC ($\approx 0.89/0.809 \text{ V}$), MgO-NC ($\approx 0.9/0.813 \text{ V}$), and comparable to the benchmark Pt/C ($\approx 0.97/0.869 \text{ V}$), respectively (Fig. 4b). This result originated from the nanostructure tuning which generated O-O bonding at the catalyst surface, the distortion at heterojunction, and the synergistic effect from

MgO and VN in heterostructure. In addition, we carried out the LSV measurement at different rotation speeds from 400 to 2500 rpm for all electrocatalysts and the results are shown in Fig. 4c and Fig. S13. The Koutechy-Levich (K-L) plots derived from LSV quantify the concentration of dissolved oxygen and reveal the electron transfer number (n) is ≈ 4 for all electrocatalysts (Fig. 4d & S14), demonstrating the complete conversion of O_2 directly to OH^- via a four-electron pathway.

In order to evaluate the catalytic kinetic activities, we derived the Tafel plot from the LSV of all as-obtained catalysts. The VM-NC showed the lowest Tafel slope value of $\approx 68.08 \text{ mV dec}^{-1}$ for ORR (Fig. S15), which is comparative to the benchmark Pt/C ($\approx 63.77 \text{ mV dec}^{-1}$), and superior to the counterparts of VN-NC ($\approx 90.40 \text{ mV dec}^{-1}$) and MgO-NC ($\approx 72.06 \text{ mV dec}^{-1}$). In addition, the electrical conductivities of electrode and the charge transfer at the electrode/electrolyte interface could be estimated by electrochemical impedance spectroscopy (EIS). As shown in Fig. S16, the charge-transfer resistance (R_{ct}) of the optimal VM-NC displayed a small value of $\approx 0.85 \Omega$, which is better than Pt/C ($\approx 0.91 \Omega$), MgO-NC ($\approx 1.03 \Omega$), and VN-NC ($\approx 1.52 \Omega$), respectively. To further understand the ORR kinetic of VM-NC catalyst, the LSV was performed using an RRDE (Fig. 4e). The H_2O_2 yield was calculated from the LSV polarization curves in the potential range of 0.3–0.7 V vs. RHE, illustrating a small value of around 12–19% (Fig. 4f). The excellent selectivity of VM-NC catalysts for ORR is superior to VN-NC (35–49%), MgO-NC (24–38%), and comparative to the state-of-the-art Pt/C catalyst (10–15%). To utilize for industrial application, the long-term stability of the electrocatalyst plays a vital role. The chronoamperometric test of VM-NC and the benchmark Pt/C catalysts are measured and illustrated in Fig. S17. The relative current density of Pt/C was decreased to 21% after 13 h, whereas the VM-NC presented excellent stability after 28 h with a negligible reduction in current density. In another hand, the VM-NC catalyst shows high tolerance toward methanol stability (Fig. S18),

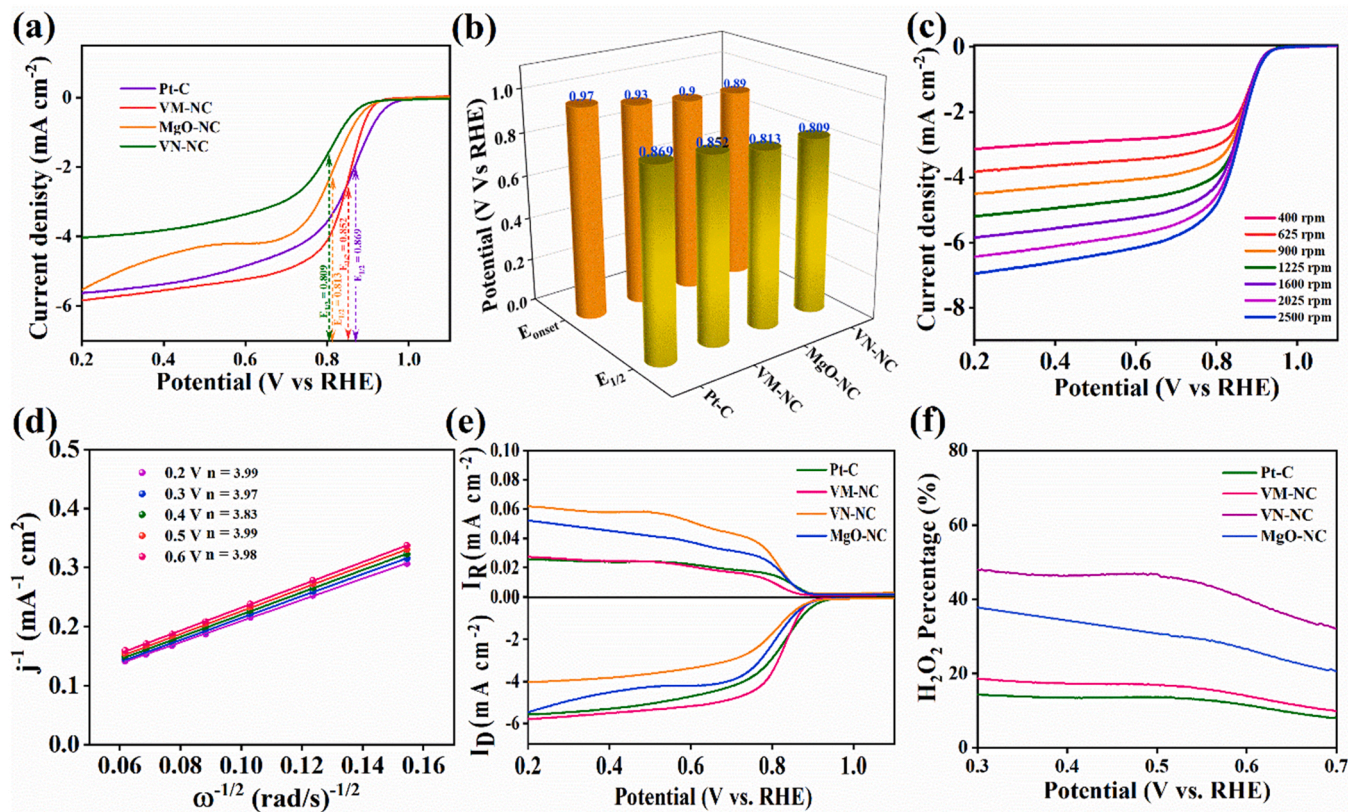


Fig. 4. Electrochemical performance of ORR (a) Polarization LSV curve at constant 1600 rpm for as-prepared catalyst, (b) Bar diagram of half wave potential of as-synthesized samples, (c) LSV curves with varying rpm from 400 to 2500 of VM-NC heterostructure, (d) K-L plots of VM-NC heterostructure, (e) LSV curves of as-synthesized electrocatalyst using RRDE, and (f) H_2O_2 percentage of as-synthesized electrocatalyst.

which is better than the Pt/C catalyst, indicating the outstanding resistance to catalytic poisoning. These excellent ORR catalysts originated from the optimal heterostructures formation of VM-NC which could enhance the active sites and reduce the adsorption energy of the intermediate species and therefore increase the ORR performance.

To apply the catalyst as the air-cathode for Zn air cells (ZACs), the OER performance was performed. The LSV polarization curves of all as-obtained catalysts were shown in Fig. 5a. The VM-NC catalyst displayed an overpotential of ≈ 253 mV at a current density of 10 mA cm^{-2} , which is superior to other comparative catalysts including the benchmark RuO_2 (≈ 320 mV), VN-NC (≈ 290 mV), and MgO-NC (≈ 340 mV). Even at a high current density of 100 mA cm^{-2} , the VM-NC catalyst required a low overpotential of ≈ 410 mV, which is outperformed than VN-NC (≈ 460 mV), MgO-NC (≈ 520 mV), and the benchmark RuO_2 (≈ 500 mV), respectively (Fig. 5b). Similarly, the Tafel slope of VM-NC catalyst was estimated from the LSV curves and represented a small value of $\approx 83.8 \text{ mV dec}^{-1}$, which is better than VN-NC ($\approx 95.4 \text{ mV dec}^{-1}$), MgO-NC ($\approx 96.3 \text{ mV dec}^{-1}$), and RuO_2 (92 mV dec^{-1}), respectively (Fig. 5c). To investigate the electrochemical active surface area (ECSA), we performed the CV measurement at various scan rate from 5 to 100 mV s^{-1} for all electrocatalysts at the non-redox peak region from 0.1 to 1.1 V vs. RHE (Fig. S19). The double-layer capacitance (C_{dl}) for VM-NC was estimated as high as 29.3 mF cm^{-2} , which is higher than the comparative catalysts of MgO-NC (19.1 mF cm^{-2}) and VN-NC (9.5 mF cm^{-2}), demonstrating the higher ECSA of heterogenous catalyst.

To examine the electrical conductivities and interfacial charge-transfer resistance of all as-prepared catalysts, the EIS measurement was performed. The VM-NC catalyst displays the smallest R_{ct} of $\approx 0.83 \Omega$, demonstrating the fast charge transfer and is favorable for OER kinetics (Fig. 5d). To successfully employ the bifunctional catalyst to practical application, the long-term stability of as-prepared catalysts

were examined using a chronoamperometric test for 80 h (Fig. 5e,f). The VM-NC exhibited a high stability with a small change of current density, illustrating the excellent performance in compared to the commercial RuO_2 and recently reported literature (Table S6) [61,62]. In addition, the morphology of VM-NC was investigated after durability test, which displayed no major structural changes occurring in the VM-NC catalyst (Fig. S20). These results indicate that VM-NC heterostructure catalyst is a promising candidate for Zn air battery with the bifunctional activity of OER and ORR.

2.5. Zinc-air battery performance

Gaining benefit from the excellent bifunctional catalytic performance for ORR and OER, we constructed the aqueous zinc-air cells (AZAC) with VM-NC catalyst as the air-cathode, zinc foil as an anode, and 3 M KOH with $\text{Zn}(\text{ac})_2$ as the electrolyte (Fig. 6a) [63]. The mixture of Pt/C and RuO_2 was coated on the carbon cloth and employed as the air cathode for comparison. The i-t polarization curve was recorded to investigate the power density of AZAC at different applied current density. Surprisingly, VM-NC based AZAC displays the highest power density of $\approx 165 \text{ mW cm}^{-2}$ at the current density of 250 mA cm^{-2} (Fig. 6b), which surpasses those of the benchmark Pt/C/ RuO_2 based AZAC (142 mW cm^{-2} at 210 mA cm^{-2}). Moreover, the discharge capacity of the AZACs was evaluated with the consumption of Zn foil, the VM-NC based AZAC showed a high specific capacity of $\approx 661 \text{ mAh g}_{\text{Zn}}^{-1}$ at a current density of 10 mA cm^{-2} , which is better than Pt/C/ RuO_2 based ZAC ($\approx 590 \text{ mAh g}_{\text{Zn}}^{-1}$) (Fig. 6c). The long-term stability test of ZAC is an important factor to evaluate the electrochemical performance of the batteries. As shown in Fig. 6d, the galvanostatic charge-discharge profile of VM-NC-based ZAC reveals a negligible change round trip voltage marginally after 400 h. Whereas the Pt/C/ RuO_2 -based ZAC exhibits a

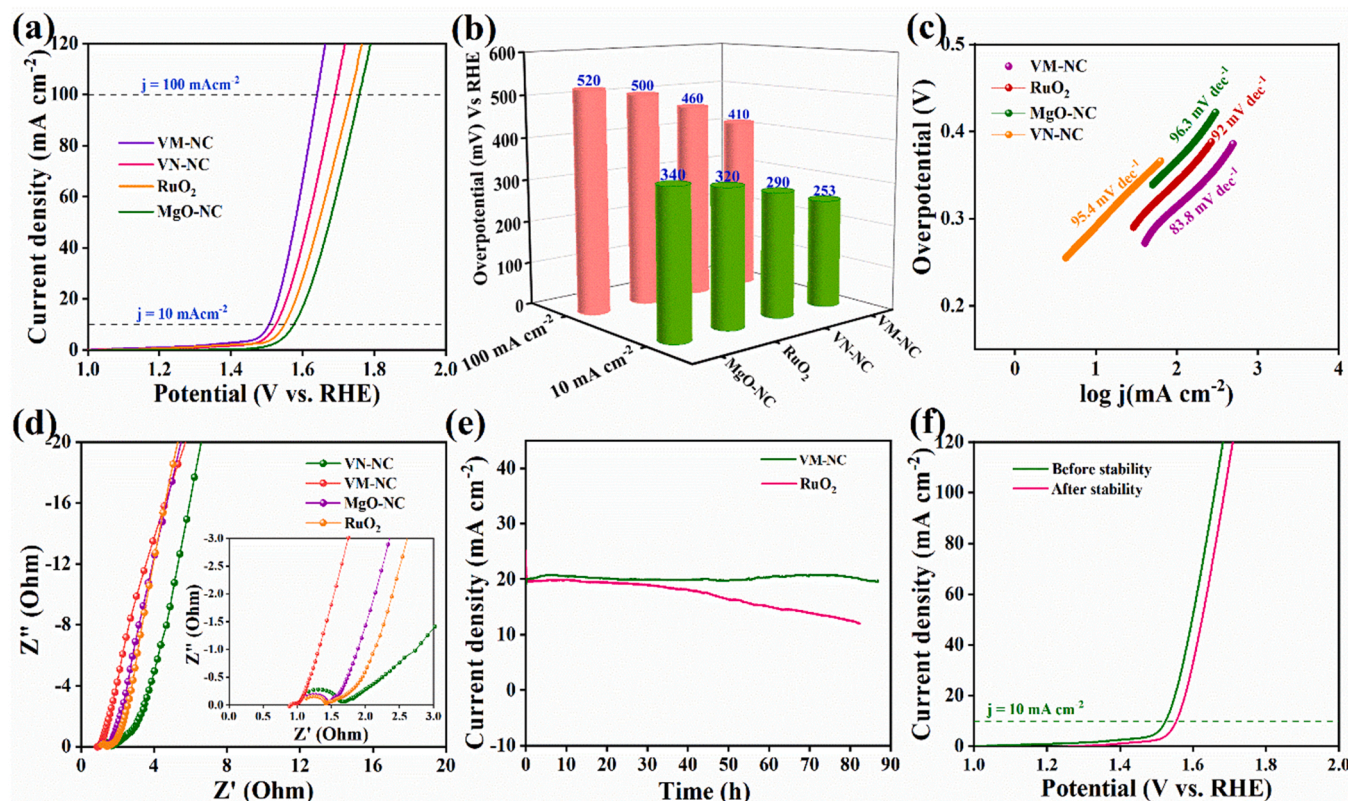


Fig. 5. Electrochemical performance of OER (a) Polarization LSV curve for as-obtained electrocatalyst (b) Bar diagram of overpotential at current density of 10 and 100 mA cm^{-2} , (c) Tafel slopes of VM-NC heterostructure and other comparatives, (d) EIS plots of VM-NC heterostructure, (e) Chronoamperometry stability of VM-NC and RuO_2 for 85 h, and (f) LSV curve after stability.

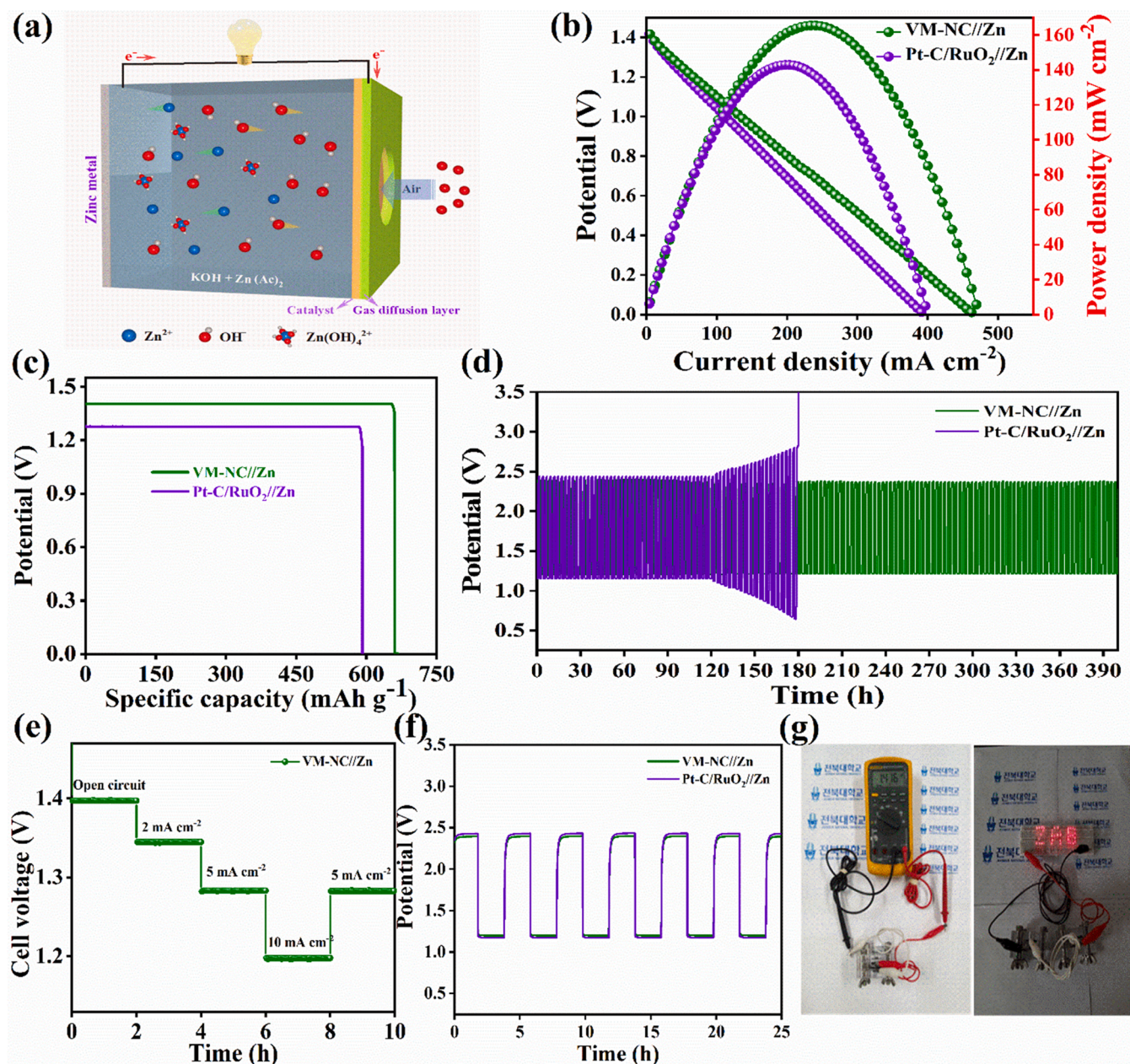


Fig. 6. Electrochemical performance of Aqueous ZAC (a) schematic illustration of assembled AZAC with VM-NC based air cathode, (b) Polarization and power density curves of AZACs, (c) The specific capacity of the VM-NC and Pt-C/RuO₂ based air cathode at 10 mA cm⁻², (d) Long term galvanostatic charge-discharge cycling of AZACs, (e) Rate performance stability of VM-NC based ZAC, (f) Initial cycles of charge-discharge of AZACs, and (g) the photograph of OCP and LED lighting with series connected VM-NC based ZACs.

significant change in voltage after 180 h. In addition, the VM-NC-based ZAC displays a high-rate performance with a stable cell voltage of 1.2 V at a current density of 10 mA cm⁻² (Fig. 6e-f). The open circuit voltage of ZAC was confirmed as high as 1.416 V and two series-connected ZAC could power the numerous LED as shown in Fig. 6g. The post-morphological characterization (SEM and TEM) was analyzed to further confirm the long-term durability of the catalysts after a long cycling performance. As shown in Fig. S21, there are negligible changes in the original structure, demonstrating the highly stable of as-prepared catalysts for ZACs application.

Flexible devices are important for wearable devices in modern life [64]. We assembled and investigated the flexible quasi-solid state pouch cell (FQSS-PC) ZACs by VM-NC (cathode), Zn foil (anode), and PVA-KOH containing 0.2 M Zn (CH₃COO)₂ as a gel electrolyte, the assembly process was shown in Fig. 7a. The assembled VM-NC based

FQSS-PC ZAC delivers the open circuit potential up to 1.4 V (Fig. S22), which is higher than the Pt-C/RuO₂-based ZACs. Moreover, the VM-NC FQSS-PC ZAC displays a high specific capacity of ≈ 598 mAh g_{Zn}⁻¹ at a current density of 10 mA cm⁻² which is superior to Pt-C/RuO₂ based ZAC (550 mAh g_{Zn}⁻¹) (Fig. 7b). The power density of FQSS-PC ZAC was examined using the i-t polarization technique, which is presented in Fig. 7c. The VM-NC FQSS-PC ZAC delivers an excellent power density of ≈ 145 mW cm⁻² at current density of 205 mA cm⁻² which is superior to that of the Pt-C/RuO₂ based ZACs (≈ 123 mW cm⁻²) and the recent reports in the literature (Table S7). In addition, the VM-NC FQSS-PC ZAC exhibits superb long-term charge-discharge durability with the energy efficiency of ($\approx 52\%$) for 100 h (Fig. 7d). To further confirm the practical application of VM-NC FQSS-PC ZAC, we performed the charge-discharge performance at different bending state (Fig. 7e). The stable charge-discharge shape confirmed the high mechanical properties of

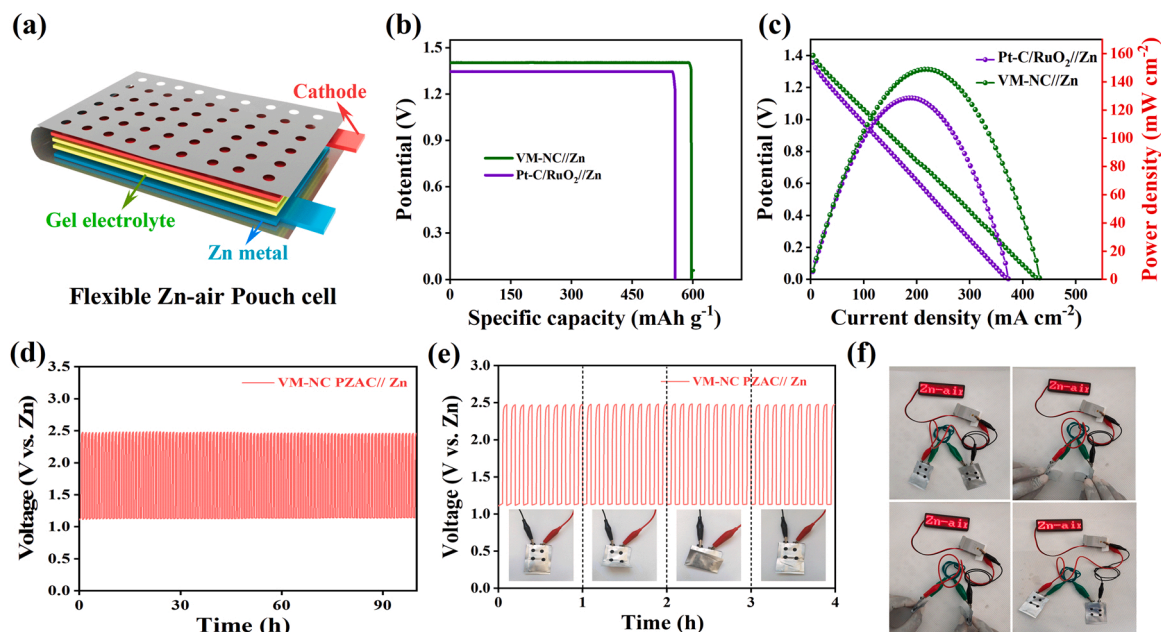


Fig. 7. Electrochemical performance of Flexible QSS-PC ZAC (a) schematic illustration of assembled PCZAC with VM-NC based air cathode, (b) The specific capacity of the VM-NC and Pt/C/RuO₂ based air cathode at 10 mA cm⁻², (c) Polarization and power density curves of PCZAC, (d) Long term galvanostatic charge-discharge cycling of PCZAC, (e) Cycling performance of VM-NC based PCZAC with different bending angles, and (f) the photograph of LED lighting with series connected VM-NC based PCZACs.

FQSS-PC ZAC without any disturbance. Moreover, a series-connected device was assembled and successfully power the LEDs at different bending state of FQSS-PC VM-NC ZACs (Fig. 7f). These excellent mechanical and electrochemical properties of FQSS-PC VM-NC ZACs suggest the prospects for the next-generation wearable electronic devices.

3. Conclusion

In summary, we successfully demonstrated a facile approach for the fabrication of well-defined VN/MgO heterojunctions on NC networks via interfacial and enriched defect engineering and employed it as an efficient bifunctional electrocatalyst for oxygen reactions and rechargeable Zn air cells. The VN/MgO-NC nanostructure exhibits a strong synergetic interaction between metals and NC networks, leading to numerous active sites and excellent conductivity. The VN/MgO-NC catalyst shows exceptional ORR performance with a high half potential (≈ 0.852 V) and a low Tafel slope ≈ 68.08 mV dec⁻¹ which is comparable to the commercial Pt/C catalyst. When it was used for OER, the VN/MgO-NC catalyst required a small overpotential of ≈ 253 mV at a current density of 10 mA cm⁻². Notably, aqueous ZAC displays a high peak power density (≈ 165 mW cm⁻²) and excellent specific capacity (≈ 691 mAh g_{Zn}⁻¹), which is comparable to the benchmark Pt/C/RuO₂ based ZAC. Furthermore, the flexible ZAC presented excellent mechanical properties with a highly electrochemical performance, outperforming to the Pt/C/RuO₂ based battery. The current work offers a new pathway to developing the enriched heterojunction catalyst as an efficient bifunctional oxygen reaction catalyst for energy storage and conversion systems.

4. Experimental section

4.1. Synthesis of VM-NC heterostructure

The chemicals and reagents were purchased from Sigma-Aldrich and directly used without purification. Firstly, 0.3 g of glucose and 5 g of dicyanamide were dissolved in water with constant stirring to form a homogeneous mixture. Next, 0.25 mmol of VCl₃ and 0.25 mmol of

MgSO₄·0.7 H₂O were separately dissolved in DI water and slowly added to the above mixture. The mixture was heated at a constant temperature of 90 °C till the water completely evaporated. Finally, the as-obtained powder was transferred to a quartz tube for further pyrolyzing at 800 °C under the protection of Ar flow. For comparison, a similar procedure was performed to obtain counterpart VN-NC and MgO-NC catalysts.

4.2. Physiochemical techniques

The XRD patterns were examined by an X-ray diffraction (Rigaku Co., D/Max 2500 V/PC). The Raman spectra and mapping were analyzed using (RAMAN touch; Nanophoton). The XPS spectrum were recorded using Theta Probe (Thermo Fisher Scientific, UK) at Korea Basic Science Institute (KBSI), Jeonju. The FE-SEM, EDAX (SUPRA 40 VP; Carl Zeiss, Germany) and a CS-TEM (JEM-ARM200, Japan) were investigated the morphological analysis and elemental compositions of the catalyst at Centre University Research Facilities (CURF), JBNU.

4.3. Electrochemical measurements

The electrochemical reduction of a catalyst was examined using an RDE and RRDE with an electrochemical workstation. The three-electrode electrochemical configuration consists of a 0.1 M KOH aqueous solution (O₂ and N₂-saturated) as the electrolyte, graphite rod as the counter electrode, Hg/HgO as the reference electrode, the catalysts loading of 0.1 mg cm⁻² droplet on glassy carbon rotating disk as the working electrode. Typically, a homogeneous catalyst ink was prepared by mixing 5 mg VM-NC catalyst in 950 μ L of isopropanol, and 40 μ L of Nafion binder under ultrasonication. The prepared ink was dropped on the RRDE and RDE, which allowed drying at room temperature. The commercial Pt/C (20 wt%) and RuO₂ were prepared as the comparison catalysts. The CV was measured in N₂ and O₂-saturated 0.1 M KOH electrolytes at a constant scan rate of 5 mV s⁻¹. LSV polarizations were performed for ORR (0.2–1 V vs. RHE) and OER (1–2 V vs. RHE) with a scan rate of 5 and 1 mV s⁻¹.

All the potentials were converted to RHE potential calculated using

the Nernst equation [65]:

$$E_{\text{RHE}} = E_{\text{Hg/HgO}} + E^{\circ}_{\text{Hg/HgO}} + (0.059 \times \text{pH}).$$

The K–L plots are derived from plots of i_d^{-1} and the inverse of square root of the rotation rate $\omega^{-1/2}$.

$$\frac{1}{j} = \frac{1}{j_L} + \frac{1}{j_K} = \frac{1}{B\omega^{1/2}} + \frac{1}{j_K} \quad (1)$$

$$B = 0.62nF C_0 D_0^{2/3} \nu^{-1/6} \quad (2)$$

Where, j_L and j_K are measured diffusion-limiting and kinetic-limiting current density B is a constant, and ω is angular velocity of the RDE (rad s^{-1}) [66–68].

4.4. Fabrication of zinc-air cells

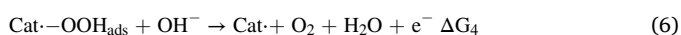
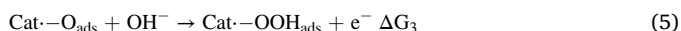
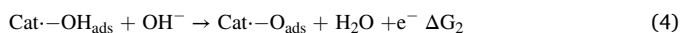
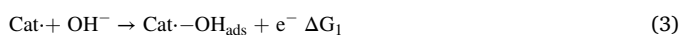
The performance of the zinc-air cells was evaluated by a Gamry potentiostat Reference 3000 and a battery testing system (WonATech) in a handmade cell. The zinc-air cells are assembled with an air cathode which is made from the catalyst coated on carbon cloth with gas diffusion layer, an anode (Zn foil), and an electrolyte (aqueous and gel electrolyte). For the preparation of PVA-gel electrolyte, 5 g of PVA and 1.8 g of Zn (ac_2) were dissolved in 50 mL of 6 M KOH and keep stirring at 85 °C overnight. Then, the obtained solution was cast on the glass petri-dish and allow it to freeze at -20 °C to obtain the gel-electrolyte [69]. The ink solution of cathode was made and dropped on the carbon cloth with the mass loading of 1 mg cm^{-2} and dried overnight. The specific capacity was determined from the galvanostatic discharge curve based on the consumption of Zn. The durability test was examined using galvanostatic charge-discharge cycles with 30 min charge followed by 30 min discharge for each cycle.

4.5. Computational methodology

In this study, we implemented first-principles calculations based on density functional theory (DFT) by using VASP 5.3 package [70,71]. The generalized gradient approximation (GGA) of Perdew, Burke, and Ernzerhof (PBE) [72], and projector augmented wave (PAW) potentials were used. In all computations, the kinetic energy cut-off is set to be 500 eV in the plane-wave expansion. For geometry optimization, $4 \times 4 \times 4$ Monkhorst-Pack k-meshes were adopted [73]. All the layer structures are fully relaxed until energy and forces are converged to $10 - 5 \text{ eV}$ and $0.01 \text{ eV } \text{\AA}^{-1}$, respectively. For the analysis of bonding in extended structures, we employed LOBSTER program [74–76], which allows the mapping of molecular orbitals based on crystal orbital Hamilton population (COHP) are employed to characterize the nature of frontier bands. Vacuum layers were set around 20 \AA in z-directions to avoid interaction between slabs. For slab calculations, k-point sampling of the Brillouin zone was obtained using a $4 \times 4 \times 1$ grid centered at the gamma (Γ) point using Monkhorst Pack Scheme. All calculations were spin-polarized and done until the force of the system converged to about 0.02 eV/\AA . Grimme's DFT-D2 functional was used to correct the dispersion forces.

4.6. DFT calculation method of OER and ORR activity

For the OER calculation, we used a four electron-mechanism to clarify the alkaline OER process. The OER mechanism in alkaline condition can be described according to the following reactions [77,78]:



where $\text{Cat}-\text{OH}_{\text{ads}}$, $\text{Cat}-\text{O}_{\text{ads}}$, $\text{Cat}-\text{OOH}_{\text{ads}}$ are intermediate species adsorbed on the active sites of catalyst and ΔG_1 , ΔG_2 , ΔG_3 , and ΔG_4 are Gibbs free energy changes in each reaction step. Theoretical overpotentials (η) of all considered structures were calculated by the following equations:

$$\eta_{\text{OER}} = \frac{\max\{\Delta G_1, \Delta G_2, \Delta G_3, \Delta G_4\}}{e} - 1.23(\text{V}) \quad (7)$$

The change in free energy is calculated by the following formula:

$$\Delta G = \Delta E + \Delta E_{\text{ZPE}} - T\Delta S$$

CRediT authorship contribution statement

Ravichandran Balaji: Conceptualization, Methodology, Investigation, Validation, Formal analysis, Writing – original draft. **Thanh Tuan Nguyen:** Methodology, Data curation, Formal analysis, Visualization, Writing – original draft. **Muthu Austeria P:** DFT calculation and explanation. **Do Hwan Kim:** DFT calculation and explanation. **Nam Hoon Kim:** Conceptualization, Writing – review & editing, Supervision. **Joong Hee Lee:** Conceptualization, Writing – review & editing, Supervision, Project administration.

Declaration of Competing Interest

The authors declare that they have no known competing financial interests or personal relationships that could have appeared to influence the work reported in this paper.

Data Availability

Data will be made available on request.

Acknowledgements

This work was supported by the Basic Science Research Program (2019R1A2C1004983) and the Regional Leading Research Center Program (2019R1A5A8080326) through the National Research Foundation funded by the Ministry of Science and ICT of Republic of Korea.

Appendix A. Supporting information

Supplementary data associated with this article can be found in the online version at [doi:10.1016/j.apcatb.2023.122895](https://doi.org/10.1016/j.apcatb.2023.122895).

References

- [1] W. Sun, F. Wang, B. Zhang, M. Zhang, V. Küpers, X. Ji, C. Theile, P. Bieker, K. Xu, C. Wang, A rechargeable zinc-air battery based on zinc peroxide chemistry, *Science* 371 (2021) 46–51.
- [2] J.-S. Lee, S. Tai Kim, R. Cao, N.-S. Choi, M. Liu, K.T. Lee, J. Cho, Metal-air batteries with high energy density: Li-air versus Zn-air, *Adv. Energy Mater.* 1 (2011) 34–50.
- [3] S.S. Shinde, J.Y. Jung, N.K. Wagh, C.H. Lee, D.-H. Kim, S.-H. Kim, S.U. Lee, J.-H. Lee, Ampere-hour-scale zinc-air pouch cells, *Nat. Energy* 6 (2021) 592–604.
- [4] D. Yu, Y. Ma, F. Hu, C.-C. Lin, L. Li, H.-Y. Chen, X. Han, S. Peng, Dual-sites coordination engineering of single atom catalysts for flexible metal-air batteries, *Adv. Energy Mater.* 11 (2021) 2101242.
- [5] T. Wang, M. Liu, S. Chaemchuen, J. Wang, Y. Yuan, C. Chen, A. Qiao, F. Verpoort, Z. Kou, Constructing a stable cobalt-nitrogen-carbon air cathode from coordinatively unsaturated zeolitic-imidazole frameworks for rechargeable zinc-air batteries, *Nano Res.* 15 (2022) 5895–5901.
- [6] N.K. Wagh, D.-H. Kim, S.-H. Kim, S.S. Shinde, J.-H. Lee, Heuristic iron-cobalt-mediated robust pH-universal oxygen bifunctional clusters for reversible aqueous and flexible solid-state Zn-air cells, *ACS Nano* 15 (2021) 14683–14696.
- [7] S. Kitano, T.G. Noguchi, M. Nishihara, K. Kamitani, T. Sugiyama, S. Yoshioka, T. Miwa, K. Yoshizawa, A. Staykov, M. Yamauchi, Heterointerface created on a cluster-loaded unilamellar hydroxide electrocatalysts as a highly active site for the oxygen evolution reaction, *Adv. Mater.* 34 (2022) 2110552.

- [8] Y. Qiao, M. Peng, J. Lan, K. Jiang, D. Chen, Y. Tan, Active-site engineering in dealloyed nanoporous catalysts for electrocatalytic water splitting, *J. Mater. Chem. A* 11 (2023) 495–511.
- [9] M. Wu, G. Zhang, N. Chen, Y. Hu, T. Regier, D. Rawach, S. Sun, Self-reconstruction of Co/Co₂P heterojunctions confined in N-doped carbon nanotubes for zinc–air flow batteries, *ACS Energy Lett.* 6 (2021) 1153–1161.
- [10] Y. Wang, X. Li, M. Zhang, J. Zhang, Z. Chen, X. Zheng, Z. Tian, N. Zhao, X. Han, K. Zaghib, Y. Wang, Y. Deng, W. Hu, Highly active and durable single-atom tungsten-doped NiS_{0.5}Se_{0.5} nanosheet @ NiS_{0.5}Se_{0.5} nanorod heterostructures for water splitting, *Adv. Mater.* 34 (2022) 2107053.
- [11] P.P. Dhakal, U.N. Pan, D.R. Paudel, M.R. Kandel, N.H. Kim, J.H. Lee, Cobalt–manganese sulfide hybridized Fe-doped 1T-Vanadium disulfide 3D-Hierarchical core-shell nanorods for extreme low potential overall water-splitting, *Mater. Today Nano* 20 (2022), 100272.
- [12] M.R. Kandel, U.N. Pan, D.R. Paudel, P.P. Dhakal, N.H. Kim, J.H. Lee, Hybridized bimetallic phosphides of Ni–Mo, Co–Mo, and Co–Ni in a single ultrathin-3D-nanosheets for efficient HER and OER in alkaline media, *Compos. B: Eng.* 239 (2022), 109992.
- [13] P.K.L. Tran, M.S. Kim, T.H. Nguyen, D.T. Tran, N.H. Kim, J.H. Lee, Interfacial engineering for design of novel 2D cobalt sulfide-Mxene heterostructured catalyst toward alkaline water splitting, *Funct. Compos. Struct.* 3 (2021), 045005.
- [14] L. Xu, S. Wu, X. He, H. Wang, D. Deng, J. Wu, H. Li, Interface engineering of antiperovskite Ni₃FeN/VN heterostructure for high-performance rechargeable zinc–air batteries, *Chem. Eng. J.* 437 (2022), 135291.
- [15] T. Liu, S. Zhao, Y. Wang, J. Yu, Y. Dai, J. Wang, X. Sun, K. Liu, M. Ni, In situ anchoring Co–N–C nanoparticles on Co₄N nanosheets toward ultrastable flexible self-supported bifunctional oxygen electrocatalyst enables recyclable zn–air batteries over 10 000 cycles and fast charging, *Small* 18 (2022) 2105887.
- [16] T.T. Nguyen, J. Balamurugan, K.-T. Lau, N.H. Kim, J.H. Lee, Novel cobalt-doped molybdenum oxynitride quantum dot@N-doped carbon nanosheets with abundant oxygen vacancies for long-life rechargeable zinc–air batteries, *J. Mater. Chem. A* 9 (2021) 9092–9104.
- [17] K.B. Ibrahim, T.A. Shifa, P. Moras, E. Moretti, A. Vomiero, Facile electron transfer in atomically coupled heterointerface for accelerated oxygen evolution, *Small* 19 (2023) 2204765.
- [18] T. Wang, P. Wang, W. Zang, X. Li, D. Chen, Z. Kou, S. Mu, J. Wang, Nanoframes of Co₃O₄–Mo₃N heterointerfaces enable high-performance bifunctionality toward both electrocatalytic HER and OER, *Adv. Funct. Mater.* 32 (2022) 2107382.
- [19] R.-Q. Li, Q. Liu, Y. Zhou, M. Lu, J. Hou, K. Qu, Y. Zhu, O. Fontaine, 3D self-supported porous vanadium-doped nickel nitride nanosheet arrays as efficient bifunctional electrocatalysts for urea electrolysis, *J. Mater. Chem. A* 9 (2021) 4159–4166.
- [20] D. Liu, H. Ai, J. Li, M. Fang, M. Chen, D. Liu, X. Du, P. Zhou, F. Li, K.H. Lo, Y. Tang, S. Chen, L. Wang, G. Xing, H. Pan, Surface reconstruction and phase transition on vanadium–cobalt–iron trimetal nitrides to form active oxyhydroxide for enhanced electrocatalytic water oxidation, *Adv. Energy Mater.* 10 (2020) 2002464.
- [21] P. Chen, K. Xu, Z. Fang, Y. Tong, J. Wu, X. Lu, X. Peng, H. Ding, C. Wu, Y. Xie, Metallic Co₄N porous nanowire arrays activated by surface oxidation as electrocatalysts for the oxygen evolution reaction, *Angew. Chem.* 127 (2015) 14923–14927.
- [22] X. Sun, Y. Zhang, Y. Xiao, Z. Li, L. Wei, G. Yao, H. Niu, F. Zheng, Surface reconstruction of Co₄N Coupled with CeO₂ toward enhanced alkaline oxygen evolution reaction, *Inorg. Chem.* 61 (2022) 14140–14147.
- [23] X.F. Lu, Y. Chen, S. Wang, S. Gao, X.W. Lou, Interfacial manganese oxide and cobalt in porous graphitic carbon polyhedrons boosts oxygen electrocatalysis for zn–air batteries, *Adv. Mater.* 31 (2019) 1902339.
- [24] J. Song, Y. Chen, H. Huang, J. Wang, S.-C. Huang, Y.-F. Liao, A.E. Fetohi, F. Hu, H.-y Chen, L. Li, X. Han, K.M. El-Khatib, S. Peng, Heterointerface engineering of hierarchically assembling layered double hydroxides on cobalt selenide as efficient trifunctional electrocatalysts for water splitting and zinc–air battery, *Adv. Sci.* 9 (2022) 2104522.
- [25] Y. Sun, K. Mao, Q. Shen, L. Zhao, C. Shi, X. Li, Y. Gao, C. Li, K. Xu, Y. Xie, Surface electronic structure modulation of cobalt nitride nanowire arrays via selenium deposition for efficient hydrogen evolution, *Adv. Funct. Mater.* 32 (2022) 2109792.
- [26] X. Zheng, X. Han, Y. Cao, Y. Zhang, D. Nordlund, J. Wang, S. Chou, H. Liu, L. Li, C. Zhong, Y. Deng, W. Hu, Identifying dense NiSe₂/CoSe₂ heterointerfaces coupled with surface high-valence bimetallic sites for synergistically enhanced oxygen electrocatalysis, *Adv. Mater.* 32 (2020) 2000607.
- [27] L. Ji, Y. Wei, P. Wu, M. Xu, T. Wang, S. Wang, Q. Liang, T.J. Meyer, Z. Chen, Heterointerface engineering of Ni₃P–Co₂P nanoframes for efficient water splitting, *Chem. Mater.* 33 (2021) 9165–9173.
- [28] Y. Hao, D. Yu, S. Zhu, C.-H. Kuo, Y.-M. Chang, L. Wang, H.-Y. Chen, M. Shao, S. Peng, Methanol upgrading coupled with hydrogen product at large current density promoted by strong interfacial interactions, *Energy Environ. Sci.* 16 (2023) 1100–1110.
- [29] P.-C. Chen, M. Liu, J.S. Du, B. Meckes, S. Wang, H. Lin, V.P. Dravid, C. Wolverton, C.A. Mirkin, Interface and heterostructure design in polyelemental nanoparticles, *Science* 363 (2019) 959–964.
- [30] X. Yang, X. Zheng, H. Li, B. Luo, Y. He, Y. Yao, H. Zhou, Z. Yan, Y. Kuang, Z. Huang, Non-noble-metal catalyst and Zn/graphene film for low-cost and ultra-long-durability solid-state zn–air batteries in harsh electrolytes, *Adv. Funct. Mater.* 32 (2022) 2200397.
- [31] S. Guo, J. Wang, Y. Sun, L. Peng, C. Li, Interface engineering of Co₃O₄/CeO₂ heterostructure in-situ embedded in Co/N-doped carbon nanofibers integrating oxygen vacancies as effective oxygen cathode catalyst for Li–O₂ battery, *Chem. Eng. J.* 452 (2023), 139317.
- [32] G. Mu, G. Wang, Q. Huang, Y. Miao, D. Wen, D. Lin, C. Xu, Y. Wan, F. Xie, W. Guo, R. Zou, A kinetic control strategy for one-pot synthesis of efficient bimetallic metal-organic framework/layered double hydroxide heterojunction oxygen evolution electrocatalysts, *Adv. Funct. Mater.* 33 (2023) 2211260.
- [33] F. Hu, D. Yu, M. Ye, H. Wang, Y. Hao, L. Wang, L. Li, X. Han, S. Peng, Lattice-matching formed mesoporous transition metal oxide heterostructures advance water splitting by active Fe–O–Cu bridges, *Adv. Energy Mater.* 12 (2022) 2200067.
- [34] L. Zhang, J. Zhu, X. Li, S. Mu, F. Verpoort, J. Xue, Z. Kou, J. Wang, Nurturing the marriages of single atoms with atomic clusters and nanoparticles for better heterogeneous electrocatalysis, *Interdiscip. Mater.* 1 (2022) 51–87.
- [35] T. Wang, P. Wang, Y. Pang, Y. Wu, J. Yang, H. Chen, X. Gao, S. Mu, Z. Kou, Vertically mounting molybdenum disulfide nanosheets on dimolybdenum carbide nanomeshes enables efficient hydrogen evolution, *Nano Res.* 15 (2022) 3946–3951.
- [36] X. Du, J. Huang, J. Zhang, Y. Yan, C. Wu, Y. Hu, C. Yan, T. Lei, W. Chen, C. Fan, J. Xiong, Modulating electronic structures of inorganic nanomaterials for efficient electrocatalytic water splitting, *Angew. Chem. Int. Ed.* 58 (2019) 4484–4502.
- [37] H.W. Go, T.T. Nguyen, Q.P. Ngo, R. Chu, N.H. Kim, J.H. Lee, Tailored heterojunction active sites for oxygen electrocatalyst promotion in zinc–air batteries, *Small* 19 (2023) 2206341.
- [38] L. Wang, L. Song, Z. Yang, Y.-M. Chang, F. Hu, L. Li, L. Li, H.-Y. Chen, S. Peng, Electronic modulation of metal–organic frameworks by interfacial bridging for efficient pH-universal hydrogen evolution, *Adv. Funct. Mater.* 33 (2023) 2210322.
- [39] Q. Zhang, F. Luo, X. Long, X. Yu, K. Qu, Z. Yang, N. P. doped carbon nanotubes confined WN–Ni Mott-Schottky heterogeneous electrocatalyst for water splitting and rechargeable zinc–air batteries, *Appl. Catal. B: Environ.* 298 (2021), 120511.
- [40] Q. Lu, H. Wu, X. Zheng, Y. Cao, J. Li, Y. Wang, H. Wang, C. Zhi, Y. Deng, X. Han, W. Hu, Controllable constructing janus homologous heterostructures of transition metal alloys/sulfides for efficient oxygen electrocatalysis, *Adv. Energy Mater.* 12 (2022) 2202215.
- [41] J. Song, D. Yu, X. Wu, D. Xie, Y. Sun, P. Vishniakov, F. Hu, L. Li, C. Li, M. Y. Maximov, Interfacial coupling porous cobalt nitride nanosheets array with N-doped carbon as robust trifunctional electrocatalysts for water splitting and Zn–air battery, *Chem. Eng. J.* 437 (2022), 135281.
- [42] Y. Zhang, L. Tao, C. Xie, D. Wang, Y. Zou, R. Chen, Y. Wang, C. Jia, S. Wang, Defect engineering on electrode materials for rechargeable batteries, *Adv. Mater.* 32 (2020) 1905923.
- [43] A.K. Singh, N. Yasri, K. Karan, E.P.L. Roberts, Electrocatalytic activity of functionalized carbon paper electrodes and their correlation to the fermi level derived from raman spectra, *ACS Appl. Energy Mater.* 2 (2019) 2324–2336.
- [44] R. Tang, Y. Li, S. Xie, N. Li, J. Chen, C. Gao, P. Zhu, X. Wang, Exploring the coordination change of vanadium and structure transformation of metavanadate MgV₂O₆ under high pressure, *Sci. Rep.* 6 (2016) 38566.
- [45] W. Chen, L. Mai, J. Peng, Q. Xu, Q. Zhu, Raman spectroscopic study of vanadium oxide nanotubes, *J. Solid State Chem.* 177 (2004) 377–379.
- [46] S. Karamat, R. Rawat, P. Lee, T. Tan, R. Ramanujan, W. Zhou, Structural, compositional and magnetic characterization of bulk V2O5 doped ZnO system, *Appl. Surf. Sci.* 256 (2010) 2309–2314.
- [47] Y. Cao, Z. Wang, Q. Bian, Z. Cheng, Z. Shao, Z. Zhang, H. Sun, X. Zhang, S. Li, H. Gedeon, L. Liu, X. Wang, H. Yuan, M. Pan, Phonon modes and photonic excitation transitions of MoS₂ induced by top-deposited graphene revealed by Raman spectroscopy and photoluminescence, *Appl. Phys. Lett.* 114 (2019).
- [48] X. He, Y. Tian, D. Deng, F. Chen, J. Wu, J. Qian, H. Li, L. Xu, Engineering antiperovskite Ni₄N/VN heterostructure with improved intrinsic interfacial charge transfer as a bifunctional catalyst for rechargeable zinc–air batteries, *ACS Sus. Chem. Eng.* 9 (2021) 17007–17015.
- [49] H. Yang, S. Gao, D. Rao, X. Yan, Designing superior bifunctional electrocatalyst with high-purity pyrrole-type CoN₄ and adjacent metallic cobalt sites for rechargeable Zn–air batteries, *Energy Storage Mater.* 46 (2022) 553–562.
- [50] M.S. Yun, T.H. Nguyen, D.T. Tran, N.H. Kim, J.H. Lee, Ultrasmall molybdenum-nitride nanoparticles confined carbon nanotubes hybrids for efficient overall water splitting, *Funct. Compos. Struct.* 4 (2022), 035008.
- [51] P. Zhai, Y. Zhang, Y. Wu, J. Gao, B. Zhang, S. Cao, Y. Zhang, Z. Li, L. Sun, J. Hou, Engineering active sites on hierarchical transition bimetal oxides/sulfides heterostructure array enabling robust overall water splitting, *Nat. Commun.* 11 (2020) 1–12.
- [52] W.-Z. Chen, M. Zhang, Y. Liu, X.-M. Yao, P.-Y. Liu, Z. Liu, J. He, Y.-Q. Wang, Super-hydrophilic MgO/NiCo₂S₄ heterostructure for high-efficient oxygen evolution reaction in neutral electrolytes, *Appl. Catal. B: Environ.* 312 (2022), 121432.
- [53] Y. Wan, C. Samundsett, J. Bullock, M. Hettick, T. Allen, D. Yan, J. Peng, Y. Wu, J. Cui, A. Javey, A. Cuevas, Conductive and stable magnesium oxide electron-selective contacts for efficient silicon solar cells, *Adv. Energy Mater.* 7 (2017) 1601863.
- [54] Z. Wang, R. Lin, Y. Huo, H. Li, L. Wang, Formation, detection, and function of oxygen vacancy in metal oxides for solar energy conversion, *Adv. Funct. Mater.* 32 (2022) 2109503.
- [55] J.W. Lee, T. Kshetri, K.R. Park, N.H. Kim, O.-K. Park, J.H. Lee, Covalently bonded boron nitride quantum dot and reduced graphene oxide composite electrode for highly efficient supercapacitors, *Compos. B: Eng.* 222 (2021), 109089.
- [56] Y. Zhang, L. Chen, B. Yan, F. Zhang, Y. Shi, X. Guo, Single Cu atoms confined in N-doped porous carbon networks by flash nanocomplexation as efficient trifunctional electrocatalysts for Zn–air batteries and water splitting, *Compos. B: Eng.* 253 (2023), 110575.

- [57] M.R. Abukhadra, M.G. Basyouny, A.A. AlHammadi, A.M. El-Sherbeeney, M. A. Salam, Enhanced decontamination of levofloxacin as toxic pharmaceutical residuals from water using CaO/MgO nanorods as a promising adsorbent, *Sci. Rep.* 10 (2020) 14828.
- [58] J. Zhu, S. Mu, Parsing the basic principles to build efficient heterostructures toward electrocatalysis, *Inorg. Chem. Front.* 10 (2023) 2220–2225.
- [59] D. Chen, R. Lu, R. Yu, Y. Dai, H. Zhao, D. Wu, P. Wang, J. Zhu, Z. Pu, L. Chen, J. Yu, S. Mu, Work-function-induced interfacial built-in electric fields in Os-OsSe₂ heterostructures for active acidic and alkaline hydrogen evolution, *Angew. Chem. Int. Ed.* 61 (2022) 202208642.
- [60] H. Radinger, V. Trouillet, F. Bauer, F. Scheiba, Work function describes the electrocatalytic activity of graphite for vanadium oxidation, *ACS Catal.* 12 (2022) 6007–6015.
- [61] R.B. Ghising, U.N. Pan, D.R. Paudel, M.R. Kandel, N.H. Kim, J.H. Lee, A hybrid trimetallic-organic framework-derived N, C co-doped Ni-Fe-Mn-P ultrathin nanosheet electrocatalyst for proficient overall water-splitting, *J. Mater. Chem. A* 10 (2022) 16457–16467.
- [62] D.M. Morales, M.A. Kazakova, S. Dieckhöfer, A.G. Selyutin, G.V. Golubtsov, W. Schuhmann, J. Masa, Trimetallic Mn-Fe-Ni oxide nanoparticles supported on multi-walled carbon nanotubes as high-performance bifunctional ORR/OER electrocatalyst in alkaline media, *Adv. Funct. Mater.* 30 (2020) 1905992.
- [63] J. Shi, X. Guo, S. Liu, Y. Sun, J. Zhang, Y. Liu, X. Zheng, Q. Kong, An altered nanoemulsion assembly strategy for in-situ synthesis of Co₂P/NP-C nanospheres as advanced oxygen reduction electrocatalyst for zinc-air batteries, *Compos. B: Eng.* 231 (2022), 109589.
- [64] W. Miao, X. Cao, M. Qin, E. Lv, H. Yu, X. Zhang, X. Dong, N-doping FeNi@C(Nx) core-shell nanoparticles synthesized by arc plasma as a highly efficient bifunctional electrocatalyst for all-solid zinc-air batteries, *Compos. B: Eng.* 260 (2023), 110769.
- [65] M. Singh, T.T. Nguyen, M.A. P. Q.P. Ngo, D.H. Kim, N.H. Kim, J.H. Lee, Metallic metastable hybrid 1T'/1T phase triggered Co₂P-SnS₂ nanosheets for high efficiency trifunctional electrocatalyst, *Small* 19 (2023) 2206726.
- [66] N. Logeshwaran, S. Ramakrishnan, S.S. Chandrasekaran, M. Vinothkannan, A. R. Kim, S. Sengodan, D.B. Velusamy, P. Varadhan, J.-H. He, D.J. Yoo, An efficient and durable trifunctional electrocatalyst for zinc-air batteries driven overall water splitting, *Appl. Catal. B: Environ.* 297 (2021), 120405.
- [67] G. Zhou, G. Liu, X. Liu, Q. Yu, H. Mao, Z. Xiao, L. Wang, 1D/3D Heterogeneous assembling body as trifunctional electrocatalysts enabling zinc-air battery and self-powered overall water splitting, *Adv. Funct. Mater.* 32 (2022) 2107608.
- [68] Y. Xu, P. Deng, G. Chen, J. Chen, Y. Yan, K. Qi, H. Liu, B.Y. Xia, 2D Nitrogen-doped carbon nanotubes/graphene hybrid as bifunctional oxygen electrocatalyst for long-life rechargeable zn-air batteries, *Adv. Funct. Mater.* 30 (2020) 1906081.
- [69] Q.P. Ngo, T.T. Nguyen, M. Singh, R. Balaji, N.H. Kim, J.H. Lee, Vanadium tunneling amorphous iron phosphate encapsulated iron phosphide on phosphorous-doped graphene promoted oxygen reactions for flexible zinc air batteries, *Appl. Catal. B: Environ.* 331 (2023), 122674.
- [70] G. Kresse, J. Hafner, Ab initio molecular dynamics for liquid metals, *Phys. Rev. B* 47 (1993) 558–561.
- [71] G. Kresse, J. Hafner, Ab initio molecular-dynamics simulation of the liquid-metal-amorphous-semiconductor transition in germanium, *Phys. Rev. B* 49 (1994) 14251.
- [72] J.P. Perdew, K. Burke, M. Ernzerhof, Generalized gradient approximation made simple, *Phys. Rev. Lett.* 77 (1996) 3865.
- [73] H.J. Monkhorst, J.D. Pack, Special points for Brillouin-zone integrations, *Phys. Rev. B* 13 (1976) 5188.
- [74] V.L. Deringer, A.L. Tchougréeff, R. Dronskowski, Crystal orbital Hamilton population (COHP) analysis as projected from plane-wave basis sets, *J. Phys. Chem. A* 115 (2011) 5461–5466.
- [75] S. Maintz, V.L. Deringer, A.L. Tchougréeff, R. Dronskowski, LOBSTER: a tool to extract chemical bonding from plane-wave based DFT, *J. Comput. Chem.* 37 (2016) 1030–1035.
- [76] S. Maintz, V.L. Deringer, A.L. Tchougréeff, R. Dronskowski, Analytic projection from plane-wave and PAW wavefunctions and application to chemical-bonding analysis in solids, *J. Comput. Chem.* 34 (2013) 2557–2567.
- [77] W. Li, C. Li, H. Dong, X. Zhang, J. Liu, M. Song, G. Wang, L. Zhao, H. Sheng, B. Chen, Expediting oxygen evolution by optimizing cation and anion complexity in electrocatalysts based on metal phosphorous trichalcogenides, *Angew. Chem.* 62 (2022), e202214570.
- [78] N.-T. Suen, S.-F. Hung, Q. Quan, N. Zhang, Y.-J. Xu, H.M. Chen, Electrocatalysis for the oxygen evolution reaction: recent development and future perspectives, *Chem. Soc. Rev.* 46 (2017) 337–365.